

## The influence of spatial and seasonal variations on the stability of the sea ice cover

TILL J.W. WAGNER\* AND IAN EISENMAN

*University of California San Diego, La Jolla, California*

### ABSTRACT

Record lows in Arctic sea ice extent are making frequent headlines in recent years. The change in albedo when sea ice is replaced by open water introduces a nonlinearity that has sparked an ongoing debate about the stability of the Arctic ice cover and the possibility of Arctic “tipping points”. Previous studies identified instabilities for a shrinking ice cover in two types of idealized models: (i) annual-mean latitudinally-varying diffusive energy balance models (EBMs) and (ii) seasonally-varying single-column models (SCMs). The instabilities in these low-order models stands in contrast with results from comprehensive global climate models (GCMs), which typically do not simulate any such instability. To help bridge the gap between low-order models and GCMs, we develop an idealized model that includes both latitudinal and seasonal variations. The model reduces to a standard EBM or SCM as limiting cases in the parameter space, thus reconciling the two previous lines of research. We find that the stability of the ice cover vastly increases with the inclusion of meridional heat transport or a seasonal cycle in solar forcing, being most stable when both are included. If the associated parameters are set to values that correspond to the current climate, then there is no instability when the climate is warmed. The two parameters have to be reduced by at least a factor of 3 for instability to occur. This implies that the sea ice cover may be substantially more stable than has been suggested in previous idealized modeling studies.

### 1. Introduction

Arctic sea ice is undergoing a striking, closely monitored, and highly publicized decline. A recurring theme in the debate surrounding this decline is the question of how stable the ice cover is. This question is often linked to the ice-albedo feedback, which is expected to be a main contributor to the rapid sea ice retreat.

The ice-albedo feedback has been studied since at least the 19<sup>th</sup> century, when James Croll investigated its importance for the climate system (Croll 1875), and it has had a central role in climate science since then. The feedback is associated with a nonlinearity in the climate system due to the jump in local albedo between ice-free and ice-covered surface conditions. This nonlinearity has long been expected to affect the stability of the climate system and potentially trigger abrupt transitions between ice-free and ice-covered regimes.

The idea of an irreversible jump from one stable state to another gained momentum when studies using idealized latitudinally-varying diffusive energy balance models (EBMs) of the annual-mean equilibrium state of the global

climate system (Budyko 1969; Sellers 1969) encountered such bistability in realistic parameter regimes (Budyko 1972; Held and Suarez 1974). These early studies were primarily concerned with the possibility of a catastrophic transition to a fully ice-covered planet, typically called the “snowball earth instability”. In addition, however, many studies showed that small polar ice covers that terminated poleward of  $\sim 70^\circ$  latitude were also typically unstable in EBMs, a feature referred to as the “small ice cap instability” (SICI) (see review in North 1984).

A bistability analogous to the SICI was found by Thorndike (1992) in a low-order single-column model (SCM) of Arctic sea ice and climate. In contrast with EBMs, this model had no representation of spatial variations, but it included seasonal variations. Modeling the sea ice seasonal cycle required representations of thermodynamic processes associated with sea ice growth and ablation. Recently, a number of studies using a range of similar SCMs identified bistability and bifurcations associated with the loss of the sea ice cover (Flato and Brown 1996; Björk 2002; Eisenman 2007; Eisenman and Wettlaufer 2009; Müller-Stoffels and Wackerbauer 2011; Abbot and Silber 2011; Moon and Wettlaufer 2011; Eisenman 2012; Moon and Wettlaufer 2012; Müller-Stoffels and Wackerbauer 2012; Björk et al. 2013).

---

\*Corresponding author address: Scripps Institution of Oceanography, University of California San Diego, 9500 Gilman Drive, La Jolla, CA 92037.

E-mail: tjwagner@ucsd.edu

The results of these EBMs and SCMs stand in contrast with results from most comprehensive global climate models (GCMs), which typically have found no stable ice-free state under current climate forcing (Hunt 1984; Tetsche et al. 2011) and simulate a smooth transition from modern conditions to a seasonally ice-free Arctic (Winton 2006; Ridley et al. 2007; Winton 2008; Armour et al. 2011; Ridley et al. 2012). In these simulations, the Arctic and Antarctic sea ice areas typically scale approximately linearly with global-mean temperature (Gregory 2002; Winton 2011; Armour et al. 2011), displaying no indication of instability. The loss of the wintertime-only sea ice cover in a very warm climate (i.e., the transition from seasonally ice-free to perennially ice-free) also occurs in a smooth and linear fashion in most GCMs (Ridley et al. 2007; Winton 2008; Armour et al. 2011). One GCM showed some evidence of nonlinearity during this transition (Winton 2008), but further analysis suggests that the nonlinearity is not sufficient to cause bistability in this case (Li et al. 2013). In contrast to comprehensive GCMs, an atmosphere-only GCM with no seasonal cycle was found to simulate bistability resembling the SICI (Langen and Alexeev 2004).

The discrepancy between the smooth ice retreat found in comprehensive GCMs and the instabilities and associated jumps in low-order models raises a pressing conundrum: Is the disagreement between the two approaches due to a fundamental misrepresentation of the underlying physics in GCMs, or is it rather a result of some aspect of the simplifications used in the idealized models? In more general terms, what physical processes dictate the stability of the sea ice cover in the global climate system? These questions are the focus of this study.

Our approach is essentially to add meridional dependence resembling an EBM to a standard SCM, thereby combining the two classes of modeling approaches. We therefore study a system that is akin to the conventional idealized models discussed above, but incorporates *both* spatial and seasonal variations. Seasonally-varying EBMs with (Bitz and Roe 2004) or without (North and Coakley 1979) representations of sea ice thermodynamic effects have been considered previously, but the influence of the seasonal cycle on the bifurcation structure has not been studied.

The article is structured as follows: in Section 2 we present the formulation of a diffusive energy balance sea ice model as motivated above. The simulated climate in the default parameter regime and its response to forcing is presented in Section 3. Section 4 discusses how the model (a) reduces to a standard EBM in the limit of no seasonal cycle and (b) reduces to a standard SCM in the limit of no horizontal heat transport. Section 5 investigates the presence of bistability as the horizontal transport and seasonal cycle parameters are varied. Conclusions are presented in Section 6.

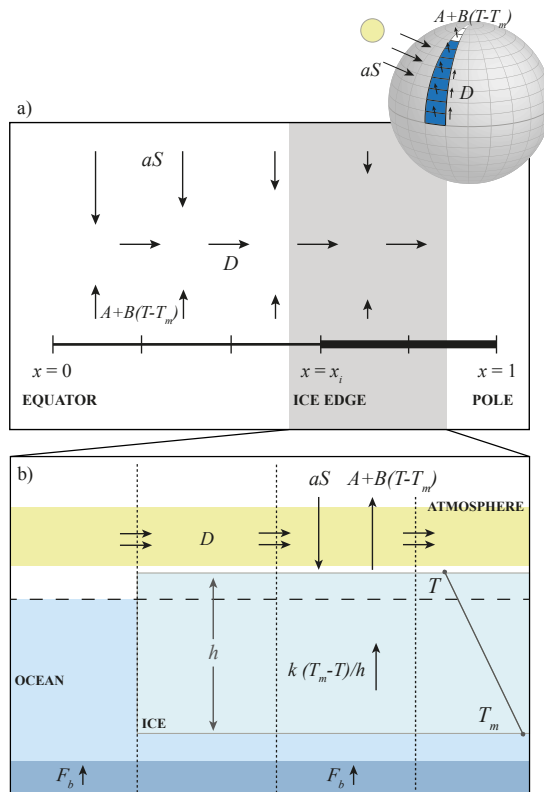


FIG. 1. Schematic of the global sea ice and climate model described in Section 2. Globe inset: Illustration of the model domain, a zonally-averaged aquaplanet. (a) Energy fluxes in the model atmosphere in the full model domain. The length of the arrows indicate decreasing solar forcing and OLR from equator to pole. (b) Energy fluxes in the model atmosphere, sea ice, and ocean in a subset of the model domain near the ice edge.

## 2. Model of sea ice and climate

Here we derive the model used in this study, which is an idealized model of sea ice and climate including a seasonal cycle and latitudinal variations with a global domain. The surface is a zonally-averaged aquaplanet with an ocean mixed layer that includes sea ice when conditions are sufficiently cold.

### a. Representation of model state

SCMs typically compute the seasonally-varying sea ice thickness,  $h(t)$ , as a prognostic variable. The surface temperature of the ice,  $T$ , is calculated diagnostically based on  $h$  and the surface flux forcing. When the ice thickness reaches zero, SCMs typically evolve the temperature of an ocean mixed layer of fixed depth (Thorndike 1992, and later studies). This temperature is taken to be vertically uniform and hence equal to the surface temperature,  $T$ . In order to evolve both ice thickness when ice is present and ocean mixed layer temperature when ice is not present, an

SCM can evolve the surface enthalpy  $E(t)$ , which is defined as (Eisenman and Wettlaufer 2009),

$$E \equiv \begin{cases} -L_f h & E < 0 \quad (\text{sea ice}), \\ c_w (T - T_m) & E \geq 0 \quad (\text{open water}). \end{cases} \quad (1)$$

$L_f$  is the latent heat of fusion of sea ice, and  $c_w$  is the heat capacity of the ocean mixed layer, which is defined as the product of the ocean mixed layer specific heat, density, and depth. The melting point,  $T_m$ , is approximated to be constant at its freshwater value. The default values for all model parameters are discussed in Section 2c and summarized in Table 1.

Standard EBMs, by contrast, compute the equilibrium value of the spatially-varying surface temperature,  $T(x)$ . Here  $x \equiv \sin \theta$  with  $\theta$  being latitude such that  $x = 0$  at the equator and  $x = 1$  at the North Pole. The aquaplanet climate that we model has identical seasonal cycles in both hemispheres, so the global climate is determined by the domain  $0 \leq x \leq 1$ .

The model developed here evolves the surface enthalpy as a function of both time and latitude,  $E(t, x)$ . A standard SCM is represented in each latitudinal grid box, and the grid boxes are coupled via latitudinal diffusion of  $T$ , as is done in standard EBMs. The model does not include a representation of horizontal ice motion. Below, we begin by discussing the EBM formulation that will be used to give spatial dependence, and then we add an SCM representation at each latitudinal grid box. The reader who is primarily interested in the model results may skip to Section 3.

### b. EBM formulation

The time evolution of the system,  $E(t, x)$ , is determined at each latitude by the net energy flux:

$$\frac{\partial E}{\partial t} = f_0 + F, \quad (2)$$

where

$$f_0 \equiv \underbrace{aS}_{\text{solar}} - \underbrace{L}_{\text{OLR}} + \underbrace{D\nabla^2 T}_{\text{transport}} + \underbrace{F_b}_{\text{ocean heating}}, \quad (3)$$

which includes fluxes due to top-of-the-atmosphere net solar radiation,  $aS$ ; outgoing longwave radiation (OLR),  $L$ ; meridional heat transport in the atmosphere,  $D\nabla^2 T$ ; and heat flux into the model domain from the ocean below,  $F_b$  (Figure 1a). Each of these terms are discussed below. Lastly,  $F(t)$  in (2) represents a spatially-uniform, seasonally-constant radiative forcing which is varied during some model runs. Increasing  $F$  can be interpreted as an increase in atmospheric  $\text{CO}_2$ , for example, analogous to global warming scenarios in GCM simulations.

Note that most EBMs compute only the equilibrium climate state,  $\partial E / \partial t = 0$  in (2), whereas here we consider the

time-evolution of the system (North and Coakley 1979). Since we are considering an aquaplanet, and the ocean mixed layer has an effective heat capacity that is more than an order of magnitude higher than the atmosphere (North and Coakley 1979), we neglect the heat capacity of the atmospheric column.

*Solar radiation* Following North and Coakley (1979), we use an approximate representation of the insolation,

$$S(t, x) = S_0 - S_1 \cos(\omega t)x - S_2 x^2, \quad (4)$$

where  $S_0$  is the annual-mean insolation at the equator,  $S_1$  is the amplitude of the seasonal variation in insolation,  $\omega = 2\pi/\text{year}$  is the annual frequency, and  $S_2$  determines the equator-to-pole insolation gradient. Note that the spatial dependence of  $S(t, x)$  is written here without using Legendre polynomials, which have often been used in the EBM literature as they enable analytical solutions. We choose the simpler representation because the model presented here is solved numerically.

Some of the insolation is reflected back to space and the rest is absorbed. The fraction of incident solar radiation that is absorbed is called the planetary, or top-of-the-atmosphere, co-albedo (i.e., one minus albedo). It depends on factors including the solar zenith angle, clouds, and the presence of reflective ice at the surface (Lian and Cess 1977). Similar to North (1975b), we write the planetary co-albedo as

$$a(x, E) = \begin{cases} a_0 - a_2 x^2 & E > 0 \quad (\text{open water}), \\ a_i & E < 0 \quad (\text{ice}), \end{cases} \quad (5)$$

where  $a_0$ ,  $a_2$ , and  $a_i$  are empirical parameters (see Table 1). It is the discrete jump in  $a(x, E)$  at the ice edge that introduces nonlinearity and therefore the possibility of multiple states. Some studies have considered various smoothed albedo transitions between ice and water (e.g., Cahalan and North 1979; Eisenman and Wettlaufer 2009), which we eschew in this study for simplicity.

*OLR* Following Budyko (1969), we represent the OLR as a linear function of the surface temperature,

$$L = A + B(T - T_m), \quad (6)$$

where  $A$  and  $B$  are empirical parameters (Table 1).

*Heat transport* Following North (1975b), the meridional heat transport is approximated as a diffusive process for the surface temperature using a constant diffusivity,  $D$ . This effectively assumes a random wind field in the atmosphere and ignores heat transport in the ocean. Due to converging meridians on a spherical earth, meridional diffusion takes the form (North 1975b)

$$D\nabla^2 T = D \frac{\partial}{\partial x} \left[ (1 - x^2) \frac{\partial T}{\partial x} \right]. \quad (7)$$

Since the climate we model is hemispherically symmetric, there can be no heat transport across the equator. Inserting (1) with  $E > 0$  (open water) into (7) at  $x = 0$  and setting heat transport to zero yields

$$\left. \frac{\partial^2 E}{\partial x^2} \right|_{x=0} = 0. \quad (8)$$

At the pole ( $x = 1$ ), the heat transport in (7) goes to zero for any distribution of  $T$  due to converging meridians, and no boundary condition is necessary.

*Ocean heat flux* The upward heat flux ( $F_b$ ) from the deep ocean into the sea ice or ocean mixed layer, which is associated with heat flux convergence within the ocean column below the mixed layer, is crudely approximated to be constant in space and time. We choose a value of  $F_b$  appropriate for the Arctic Ocean, where there is net horizontal ocean heat flux convergence. Note that while this helps the model to accurately simulate conditions in the Arctic Ocean and retains simplicity in the model formulation, it makes the global ocean a heat source, albeit a weak one.

*EBM summary* It is convenient to rewrite (2)–(3) with the temperature-dependent and temperature-independent terms consolidated as

$$\frac{\partial E}{\partial t} = C - M(T - T_m), \quad (9)$$

with

$$C \equiv aS - A + F_b + F, \quad M \equiv B - D\nabla^2. \quad (10)$$

Note that in the absence of sea ice,  $\partial E/\partial t = c_w \partial T/\partial t$  on the left-hand side of (9). Hence this model is a fairly standard EBM with the exception that time dependence is retained and an ocean heat flux ( $F_b$ ) is included. Note also that the albedo feedback is encompassed in the dependence of  $a$  on  $E$  (5).

### c. Addition of SCM physics

Next, we add a representation of sea ice freezing and melting to the model and compute the resulting effect on the surface temperature. This is done by coupling equations (9)–(10) to an SCM representation of thermodynamic sea ice (Figure 1b). Note that the energy balance in this model is computed at the top-of-the-atmosphere, as in typical EBMs, and in contrast to typical SCMs where the energy balance is computed at the surface.

We approximately follow the SCM developed in Eisenman (2012). This SCM can be directly derived (see Eisenman and Wettlaufer 2009) as an approximate representation of the SCM of Maykut and Untersteiner (1971), which represents processes including vertical energy flux between the ice and the atmosphere ( $f_0$ ), vertical conduction of heat within the ice, vertical heat flux between the

ice and the ocean below ( $F_b$ ), basal congelation during the winter growth season, and surface and basal ablation during the summer season.

The heat conduction within the ice is governed by a diffusion equation for the internal ice temperature. In what follows, we assume that the energy associated with phase change is much larger than the energy associated with temperature change within the ice, i.e., that the relevant Stefan number,  $N_S \equiv (L_f \Delta h)/(c_i h \Delta T)$  (Eisenman 2012), satisfies  $N_S \gg 1$ . Here  $c_i$  is the specific heat of the ice. In this approximation, the solution to the diffusion equation reduces to a linear temperature profile, with temperature varying from  $T \leq T_m$  at the top surface to  $T_m$  at the bottom surface (Eisenman and Wettlaufer 2009). Note that  $N_S > 1$  for the sea ice seasonal cycle when the ice thickness is  $h < 8$  m, making this a relatively accurate approximation in the default parameter regime but less accurate when the ice is very thick (Eisenman 2012).

The heat flux upward through the ice is then equal to  $k(T_m - T)/h$ , where  $k$  is the ice thermal conductivity, which is treated here as constant. If the ocean mixed layer cools to  $T_m$ , ice begins to grow. As long as ice is present, the temperature of the ocean mixed layer is set to remain constant at  $T_m$ . In this regime, the ocean heat flux  $F_b$  goes directly into the bottom of the ice without losing heat to the ocean mixed layer.

Hence, when ice is present, the change in energy per unit area is equal to the change in  $E$ , and the ice thickness ( $h = -E/L_f$ ) evolves according to (9)–(10). In other words, (9)–(10) applies equivalently for both ice-covered and ice-free conditions. In the model results, we identify the ice edge latitude,  $\theta_i$ , as the latitude where  $E$  changes sign, and we similarly define  $x_i \equiv \sin \theta_i$ .

There are two possible regimes when ice is present: (i)  $T < T_m$ , in which case the net surface flux must be zero, and (ii)  $T = T_m$ , in which case surface melt proportional to the net surface flux occurs. We determine which case applies by computing the surface temperature that would balance the surface energy fluxes and determining whether it is above or below the melting point. We define this surface flux balance temperature as  $T_i$  for notational convenience. Solving

$$k(T_m - T_i)/h = -C + M(T_i - T_m) + F_b,$$

for  $T_i$  gives

$$T_i = T_m + \left( M - \frac{kL_f}{E} \right)^{-1} (C - F_b), \quad (11)$$

where we have used (1). We note that  $M$  is a scalar in a typical SCM but includes the Laplacian operator ( $\nabla^2$ ) in this diffusive model. If  $T_i < T_m$ , then the surface flux is balanced by a subfreezing surface temperature, and the frozen regime (i) applies, with  $T = T_i$ . On the other hand,  $T_i > T_m$  indicates that the surface flux cannot be balanced

by a subfreezing surface temperature, and surface melt (ii) occurs. In this case the surface temperature remains at the melting point,  $T = T_m$ , and the surface melt is calculated using a Stefan condition, which states that the ice thinning from surface melt is equal to the net surface flux divided by  $L_f$  (Maykut and Untersteiner 1971).

Ice-free surface conditions can be included by adding a third regime for the surface temperature as

$$T = \begin{cases} T_m + E/c_w & h = 0 & \text{(open water),} \\ T_m & h > 0, \quad T_i > T_m & \text{(melting ice),} \\ T_i & h > 0, \quad T_i < T_m & \text{(freezing ice).} \end{cases} \quad (12)$$

Note that  $T_i$  is a function of  $E$ .

Equations (9)–(12) fully determine the model, which represents the seasonally-varying global surface temperature and allows sea ice of varying thickness to form when the ocean mixed layer temperature reaches the melting point.

#### d. Default parameter values

The default values of all model parameters are given in Table 1. Values for  $D$ ,  $B$ , and  $c_w$  are adopted from North and Coakley (1979); note that  $c_w$  corresponds to a 75 m ocean mixed layer depth. The insolation parameters ( $S_0$ ,  $S_1$ , and  $S_2$ ) are calculated from the Legendre polynomial coefficients in North and Coakley (1979) and the solar constant in North (1975b). Coalbedo parameter values ( $a_0$ ,  $a_2$ , and  $a_i$ ) are adopted from North (1975b), converting their Legendre polynomial coefficients into our formalism.

For the time-averaged heat flux from below into the base of the sea ice when ice is present or the bottom of the ocean mixed layer when ice is not present,  $F_b$ , Maykut and Untersteiner (1971) use a value of  $F_b = 2 \text{ W/m}^2$  based on central Arctic observations. Thorndike (1992) adopts a possible range of  $F_b = 0 - 10 \text{ W/m}^2$ . Other observations suggest a value of  $F_b = 5 \text{ W/m}^2$  (Maykut and McPhee 1995). We adopt a value within the range of these previous estimates,  $F_b = 4 \text{ W/m}^2$ .

We use a value for the thermal conductivity,  $k$ , corresponding to pure freshwater ice. For the latent heat of ice fusion we take  $L_f = 16.4 \text{ W yr/m}^3$ , which is somewhat higher than the pure water value of  $L_f = 9.8 \text{ W yr/m}^3$ , in order to crudely account for the freezing point in the model ( $T_m$ ) not being reduced due to ocean salinity.

Lastly, we choose a value of  $A = 193 \text{ W/m}^2$ , which is approximately equal to the value in Mengel et al. (1988), in order to simulate an annual-mean global-mean temperature consistent with current observations when  $F = 0$ .

In the following simulations we vary the climate forcing,  $F$ , as well as  $D$  and  $S_1$ . For convenience, we denote the default values of the latter two parameters as  $D^*$  and  $S_1^*$  (Table 1).

TABLE 1. Default Parameter Values

	Description	Value	Unit
$D$	diffusivity for heat transport	0.6	$\text{W/m}^2/\text{K}$
$A$	OLR when $T = T_m$	193	$\text{W/m}^2$
$B$	OLR temperature dependence	2.09	$\text{W/m}^2/\text{K}$
$c_w$	ocean mixed layer heat capacity	9.8	$\text{W yr/m}^2/\text{K}$
$c_g$	diffusive ghost layer heat capacity	0.098	$\text{W yr/m}^2/\text{K}$
$\tau_g$	ghost layer coupling timescale	$3 \times 10^{-6}$	yr
$S_0$	insolation at equator	415	$\text{W/m}^2$
$S_1$	insolation seasonal variation	268	$\text{W/m}^2$
$S_2$	insolation spatial variation	240	$\text{W/m}^2$
$a_0$	ice-free co-albedo at equator	0.7	-
$a_2$	ice-free co-albedo spatial variation	0.1	-
$a_i$	co-albedo where there is sea ice	0.4	-
$F_b$	heat flux from ocean below	4	$\text{W/m}^2$
$k$	sea ice thermal conductivity	2	$\text{W/m/K}$
$L_f$	sea ice latent heat of fusion	16.4	$\text{W yr/m}^3$
$T_m$	melting temperature	0	$^\circ\text{C}$
$F$	radiative forcing	0 (varies)	$\text{W/m}^2$

#### e. Numerical solution

Numerically solving the system (9)–(12) is not straightforward due to the essentially implicit representation of  $T_i$  in (11). For a given timestep, the computation of  $T$  in regions with freezing ice requires knowledge of  $T$  at all locations for the meridional heat transport. We employ a numerical approach that solves a system of equations representing two coupled layers. Horizontal diffusion occurs in a “ghost” layer with heat capacity  $c_g$ , all other processes occur in the main layer, and the temperature of the ghost layer is relaxed toward the temperature of the main layer with timescale  $\tau_g$ . This “two-layer” system reduces to (9)–(12) in the limit that  $c_g \rightarrow 0$  and  $\tau_g \rightarrow 0$ . The details of the two-layer integration method are described in Appendix A. In the model simulations,  $c_g$  and  $\tau_g$  are chosen to be sufficiently small that further reducing their values does not significantly influence the numerical solution (values given in Table 1).

The model is solved numerically in  $0 \leq x \leq 1$  at 25 km meridional resolution (400 grid boxes, equally spaced in  $x$ ) with timestep  $\Delta t = 0.37 \text{ d}$ . The spatial resolution is required to sufficiently resolve the evolution of the sea ice cover, especially in parameter regimes where there is bistability with the cold state having an ice edge near the pole. The temporal resolution is chosen to ensure numerical stability of the solution.

### 3. Model results in the default parameter regime

In this section we discuss the simulated climate state, first in the default parameter regime with  $F = 0$ , and then in the case where the climate is warmed by increasing  $F$ .

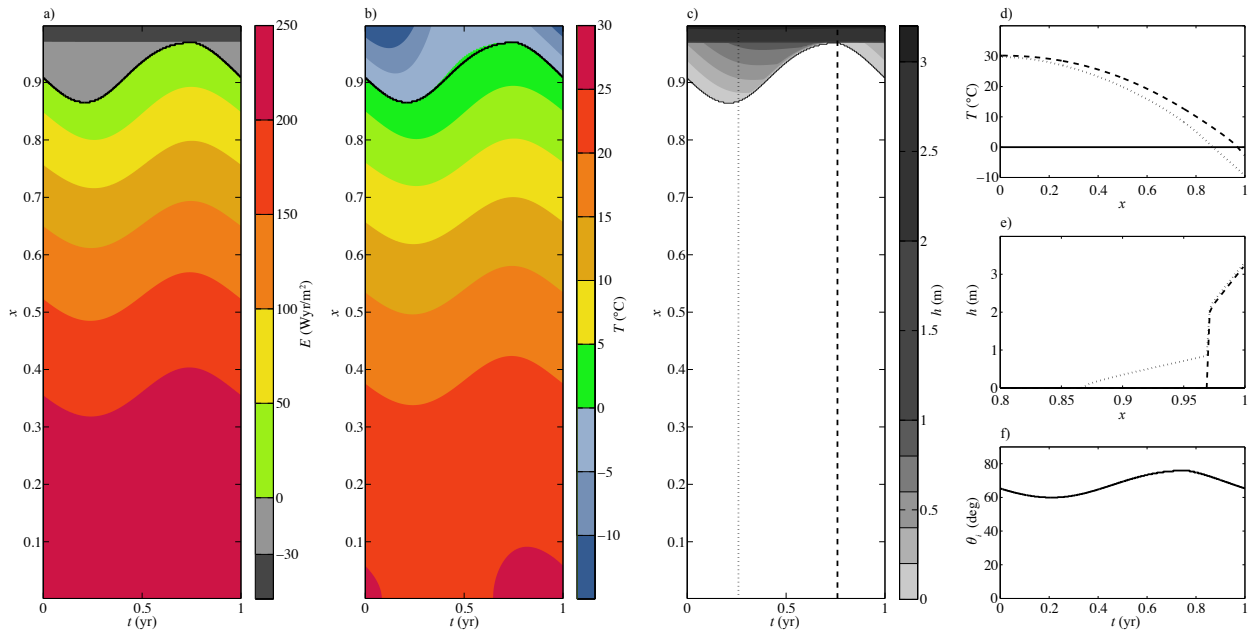


FIG. 2. Simulated climate in the default parameter regime. (a) Contour plot of seasonal cycle of surface enthalpy,  $E(x,t)$ . (b) Contour plot of seasonal cycle of surface temperature,  $T(x,t)$ . (c) Contour plot of sea ice thickness,  $h(x,t)$ . The black line in panels a, b, and c indicates the ice edge. (d) Surface temperature,  $T$  in summer and winter, corresponding to dashed and dotted vertical lines in panel c, respectively. (e) Ice thickness,  $h$ , in summer and winter in high latitudes. (f) Seasonal cycle of the latitude of the sea ice edge,  $\theta_i$ .

### a. No climate forcing ( $F = 0$ )

The simulated climate with all parameters at their default values (Table 1) is illustrated in Figure 2, where the seasonal cycle of the spun-up climate is plotted. Fig. 2a shows the seasonal cycle of  $E(t,x)$ , which fully represents the model state since  $E$  is the only prognostic variable and the forcing varies seasonally. The seasonal cycle of surface temperature (Figure 2b) and ice thickness (Figure 2c) are very roughly consistent with current climate observations in either hemisphere. The simulated surface temperature varies approximately parabolically with  $x$  from an equatorial temperature of  $\sim 29^{\circ}C$  throughout the year to a polar temperature of  $\sim -10^{\circ}C$  in winter and  $\sim -3^{\circ}C$  in summer (Figure 2d). Sea ice thickness at the pole is  $\sim 3$  m throughout the year (Figure 2e). The edge of the sea ice cover ranges from  $\theta_i \approx 60^{\circ}$  in winter to  $\theta_i \approx 78^{\circ}$  in summer (Figure 2f), which is very roughly consistent with observations of the zonal-mean ice edge latitude in the Northern Hemisphere (Eisenman 2010).

The presence of a substantial seasonal sea ice cover in the simulated climate (Figure 2c), which is qualitatively consistent with observations, stands in contrast with typical SCM results. It has been a conundrum in SCM studies that they have typically struggled to simulate a stable seasonal sea ice cover. Thorndike (1992) found that the SCM he developed was unable to simulate a stable seasonal ice cover. This SCM was forced by a square-wave seasonal cycle, with insolation switching between a con-

stant summer value for six months and a constant winter value for the other six. The SCM in Eisenman and Wettlaufer (2009), which had smoothly varying insolation and longwave radiation, did feature stable seasonal ice, albeit in a relatively small radiative forcing range. In Eisenman and Wettlaufer (2009) (their Figure S5), this stable seasonal ice was hypothesized to arise due to a larger seasonal amplitude in the longwave forcing than that used by Thorndike (1992). Moon and Wettlaufer (2012) proposed the contrasting hypothesis that the square-wave seasonal cycle in solar forcing used in Thorndike (1992) was the essential factor preventing the SCM from simulating a stable seasonal ice cover. They found that resolving the seasonal cycle in solar forcing with at least two different values during summer was necessary for stable seasonal ice.

The results presented here suggest an alternative resolution of the SCM conundrum: the inclusion of a horizontal dimension appears to be an essential ingredient for accurately simulating the stability of the seasonal ice cover. In apparent contrast with Eisenman and Wettlaufer (2009), who found a narrow forcing range that allowed for stable seasonal ice, in this model seasonal ice occurs over a wide range of latitudes. In apparent contrast with Moon and Wettlaufer (2012), who found that square-wave solar forcing did not allow seasonal ice, the model developed here still simulates a large seasonal migration of the ice edge when the  $\cos \omega t$  factor in (4) is replaced with a square wave (not shown).

Note that the seasonal change in total ice volume is almost exclusively due to the growth of a thin wedge of seasonal ice at the fringe of the perennial ice pack in the winter. The thicker ice that is found in the perennial ice pack undergoes little thickness change during the course of the year. Relatedly, all surface melt in this model is occurring in the seasonal ice region, in contrast with typical SCMs and also with observations (e.g., Maykut and Untersteiner 1971). This is due to the simulated diffusive atmospheric heat transport nearly compensating the seasonal variations in  $S$  in the perennial ice region.

#### b. Forced warming (increasing $F$ )

Next, we numerically approximate the steady-state seasonally-varying response of the model to changes in the climate forcing ( $F$ ) by slowly ramping up  $F$ . Beginning with a 200 year spin-up simulation at the initial forcing value ( $F = -10 \text{ W/m}^2$ ), we increase  $F$  in increments of  $0.2 \text{ W/m}^2$  and integrate the system for 40 years at each value of  $F$ . This approach is used in all simulations in this study of the model response to increasing or decreasing climate forcing.

As shown in Figure 3, the climate steadily warms and the seasonally-varying sea ice cover steadily recedes until the pole is ice-free throughout the year. The summer ice disappears at  $F = 3.5 \text{ W/m}^2$  and the winter ice at  $F = 9 \text{ W/m}^2$ .

It is noteworthy that there is no apparent jump at any point in the sea ice response, and there is no apparent difference in the climate response when transitioning from perennial to seasonal ice covers and then to annually ice-free conditions. Rather, the summer and winter sea ice edges both response fairly linearly to  $F$  (dashed lines in all panels of Figure 3). This linearity of the response is consistent with results from comprehensive GCMs (e.g., Winton 2006; Armour et al. 2011; Winton 2011). It is in contrast with previous results from EBMs and SCMs, as discussed above.

### 4. Bistability with no seasonal cycle or no diffusion

The two standard types of low-order models discussed above, EBMs and SCMs, both exhibit bistability of the sea ice cover in ostensibly realistic parameter regimes. These results can both be reproduced in the present model. As we will show in this section, in the limit of no seasonal cycle ( $S_1 = 0$ ), the present model reduces to a standard EBM, and in the limit of no horizontal heat transport ( $D = 0$ ), the present model reduces to standard SCMs at each spatial gridpoint.

#### a. EBM regime ( $S_1 = 0$ )

When the seasonal amplitude is set to zero in the present model ( $S_1 = 0$ ), the steady-state solution is equivalent to

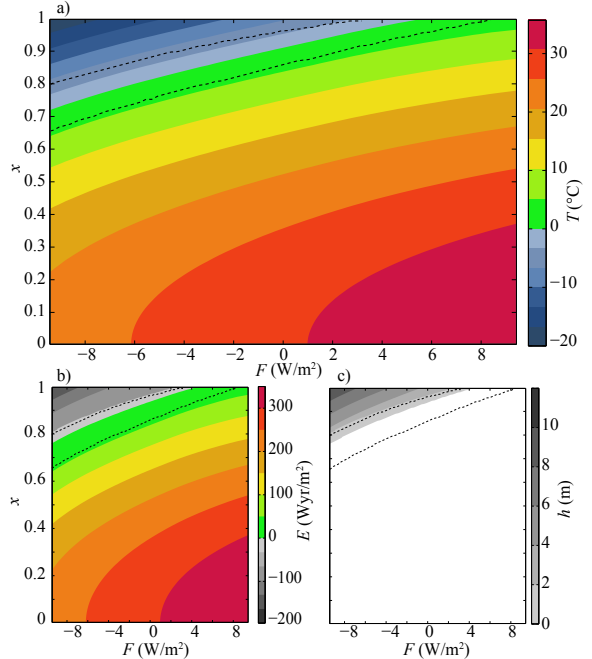


FIG. 3. Simulated warming and receding sea ice in the default parameter regime with increasing climate forcing,  $F$ . Shown are the annual-mean (a) surface temperature  $T$ , (b) surface enthalpy  $E$ , and (c) ice thickness  $h$ , as functions of location  $x$  and forcing  $F$ . Black dashed lines show the summer (above) and winter (below) locations of the sea ice edge.

the solution of a standard annual-mean EBM. In this limit, the equilibrium state of the system becomes time independent, with (9) reducing to

$$0 = C - M(T - T_m) \quad (13)$$

In this case, the time evolution of the enthalpy ( $E$ ) is no longer included, so the surface temperature can be determined directly from this ordinary differential equation in  $x$ , without consideration of the vertical heat conduction within the ice. Note that the associated ice thickness can be determined from (11) - (12).

Equation (13) is equivalent to the formulation of a standard annual-mean EBM (e.g., equation (22) in North et al. 1981). Analytical solutions can be found by making use of the property that Legendre polynomials are eigenfunctions of the diffusion operator (7) contained in  $M$ . They are, however, complicated by the dependence of the albedo on  $T$ . Following Held and Suarez (1974), we approximately solve (13) for  $F$  as a function of  $x_s$  (e.g., equations (28) - (29) and (37) in North et al. 1981). The approximate analytical solution involves a sum of even Legendre polynomials multiplied by integrals of the solar forcing ( $aS$ ), and we retain terms up to the 40th degree, similar to previous studies (e.g., Mengel et al. 1988).

Figure 4 shows both the analytical solution and numerical model results. It illustrates the evolution of the sea ice

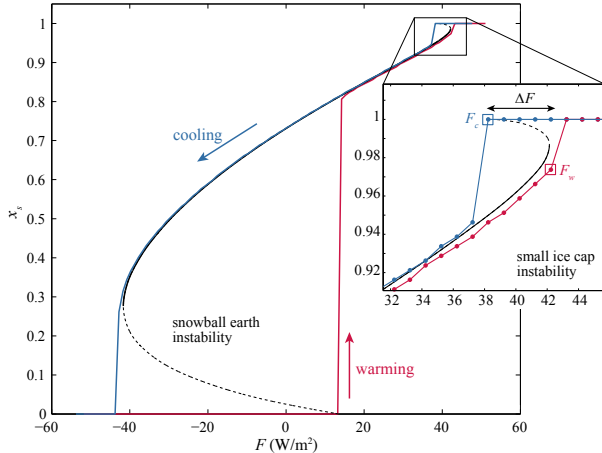


FIG. 4. Steady-state locations of the ice edge ( $x_i$ ) under varied climate forcing ( $F$ ) in the parameter regime ( $S_1 = 0$ ,  $D = D^*/6$ ). Both the “snowball earth instability” and the “small ice cap instability” are readily apparent. The analytic EBM solution is shown in black, illustrating stable states (solid) and unstable states (dashed). The numerical solution is indicated for  $F$  being slowly ramped up (red) and then back down (blue). Inset: Detail of the SICI, illustrating the definition of  $\Delta F$  as the difference between the bifurcation points  $F_c$  (blue square) and  $F_w$  (red square).

edge ( $x_i$ ) under varied climate forcing ( $F$ ) with  $S_1 = 0$  and  $D = D^*/6$ . (The diffusivity is reduced in order to enlarge the SICI region and thereby better illustrate the instability). The figure indicates the sea ice retreat as  $F$  is increased (red) until an ice-free state is reached, followed by the onset and advance of the sea ice cover when  $F$  is subsequently decreased (blue). The figure features two hysteresis loops which correspond to (i) the SICI, for  $x_i > 0.98$ , and (ii) the snowball earth instability, for  $x_i < 0.3$ . We focus on the former, which occurs in the range of climates similar to present-day and warmer. Figure 4 highlights the close agreement between numerical results (blue/red) and the analytical solution (black). It can be shown that the climates indicated in Figure 4 are stable where the slope is positive (solid) and unstable where the slope is negative (dashed) (North 1975a). The system therefore does not support an ice cover with an equilibrium ice edge poleward of  $x_i = 0.98$  or equatorward of  $x_i = 0.3$ .

A measure of the extent of bistability in the system can be obtained by considering the width of the hysteresis loop. We define two critical values of the forcing  $F$ : (i)  $F_w$  is the value at which the system transitions from an ice-covered to an ice-free pole in a warming scenario and (ii)  $F_c$  is the value at which an ice cover reappears in a cooling scenario. These two values of  $F$  are indicated in the inset of Figure 4 by a red square and a blue square, respectively. Note that a saddle-node bifurcation occurs at each of these values. The width of the hysteresis loop is then defined as

$$\Delta F \equiv F_w - F_c. \quad (14)$$

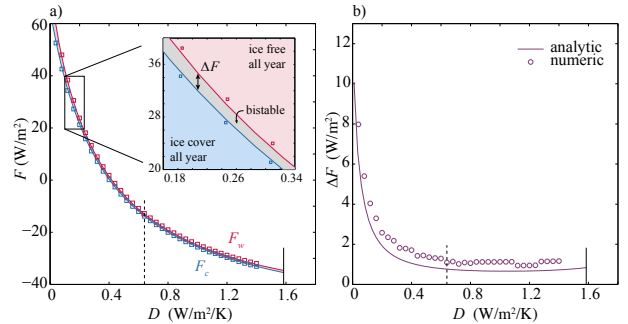


FIG. 5. Dependence of the critical forcing values on  $D$  for the case with no seasonal variation ( $S_1 = 0$ ). (a)  $F_w$  (blue) and  $F_c$  (red) versus  $D$  for numerical results (squares) and analytical results (solid). The inset indicates the bistable regime and highlights the difference between numerical and analytical approximate solutions, which become more evident for  $\Delta F$ . (b) Hysteresis width  $\Delta F$  versus  $D$  for numerical (circles) and analytical (solid) approximate solutions. Also indicated are the default value  $D = D^*$  (dashed vertical line) and the value at which the SICI merges with the snowball earth instability  $D = D_{max}$  (solid vertical line).

Note that  $\Delta F$  can be seen as a societally relevant measure of climate bistability, since it indicates how much the radiative forcing would need to be reduced for the sea ice to retreat after crossing a “tipping point” during global warming.

We begin with the simplest case, when there is no seasonal cycle ( $S_1 = 0$ ) and no heat transport ( $D = 0$ ). In this case,  $F_c$  is the forcing associated with the pole being ice-free at  $T = T_m$ , and  $F_w$  is the forcing associated with the pole being ice-covered at  $T = T_m$ . Hence the width of the hysteresis loop  $\Delta F$  is equal to the jump in solar forcing between ice-covered and ice-free conditions at the pole,

$$\Delta F = (a_0 - a_2 - a_i)(S_0 - S_2) = 35 \text{ W/m}^2, \quad (15)$$

as can also be directly shown from (2)-(5).

In the remainder of this section we consider how  $\Delta F$  depends on the magnitude of heat transport ( $D$ ) when  $S_1 = 0$ . Much of the discussion in the following sections is concerned with how  $\Delta F$  varies in other regions of the parameter space.

Polar temperatures are generally higher for larger meridional heat transport. As  $D$  increases, the sea ice cover therefore disappears and also reappears at lower values of  $F$ , i.e.,  $F_w$  and  $F_c$  both decrease. This is illustrated in Figure 5a, where the critical forcings,  $F_w$  and  $F_c$ , are plotted versus  $D$  in both the analytical and numerical model solutions. For the range of forcings  $F < F_c$ , the model does not feature SICI bistability, with the only stable state being a finite ice cover. Similarly, the range  $F > F_w$  only allows stable states with an ice-free pole. In the range  $F_c < F < F_w$  both ice-covered and ice-free conditions are stable, resulting in SICI bistability. These three regimes are illustrated in the inset of Figure 5a.

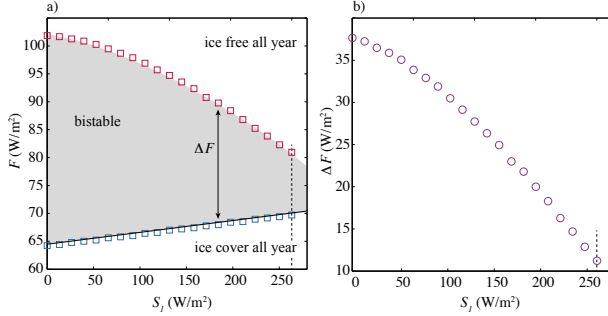


FIG. 6. Dependence of the critical forcing values on  $S_1$  for the case with no horizontal heat transport ( $D = 0$ ). (a)  $F_w$  (blue) and  $F_c$  (red) versus  $S_1$  for numerical results (squares), also including the exact analytical solution for  $F_w$  (solid). (b) Hysteresis width  $\Delta F$  versus  $S_1$  for numerical results (circles). The default parameter value,  $S = S_1^*$ , is indicated in both panels by a dashed vertical line.

The dependence of  $\Delta F$  on  $D$  is shown in Figure 5b. Note that the discrepancy between the analytical and numerical solutions is expected to arise due to numerical inaccuracy in determining the bifurcation point and diminishes with increasing spatial resolution. We find that  $\Delta F$  mostly decreases with increasing  $D$ , with the greatest sensitivity of  $\Delta F$  occurring when  $D$  is small.

This indicates that the horizontal coupling between different latitudes has a strong stabilizing effect on the polar sea ice cover in the range of  $D$  considered here. Related explanations involving the diffusive lengthscale associated with (9)–(10) have been suggested for the influence of  $D$  on the extent of the SICI (Lindzen and Farrell 1977; North 1984).

At a critical diffusivity,  $D_{max}$  (marked by a solid vertical line in Figure 5b), the small ice cap instability merges with the snowball earth instability and there is no stable climate with  $0 < x_i < 1$ . This property of EBMs in the limit  $D \rightarrow \infty$  has been noted previously (Lindzen and Farrell 1977). In this limit the global surface temperature becomes approximately isothermal, allowing only stable solutions with  $T < T_m$  everywhere or  $T > T_m$  everywhere.

### b. SCM regime ( $D = 0$ )

The present model reduces to an array of independent SCMs when meridional heat transport is turned off by setting  $D = 0$ . In this case no communication occurs between individual locations and the state of each grid point is determined by the balance of vertical heat fluxes alone. For a given value of  $x$ , (9) reduces to an ordinary differential equation in time representing a standard SCM (e.g., equation (2) in Eisenman 2012). Here the steady-state solutions are represented by the seasonal cycle of  $E$ .

The definitions of critical forcings  $F_c$  and  $F_w$  in the previous section are most readily applied to this regime by considering only the pole,  $x = 1$ . As  $F$  is ramped up, the

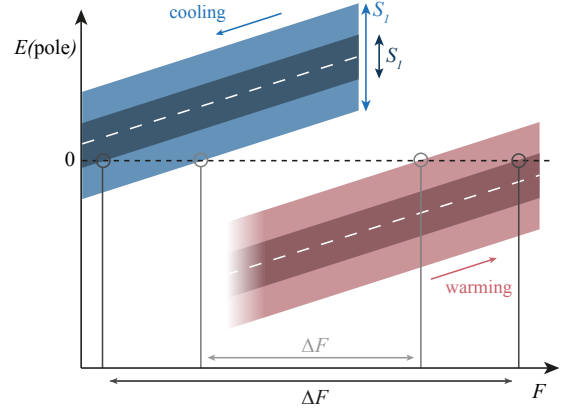


FIG. 7. Schematic illustrating the increase in  $F_c$  (the critical value of  $F$  in a cooling scenario), associated with an increase in  $S_1$  from the dark blue range to the light blue range. The reverse occurs in the warming scenario for  $F_w$  (dark red and light red). The dashed white line represents the annual mean enthalpy at the pole and the colored shading represents the seasonal range at the pole. Ice is present when  $E < 0$ . The figure also indicates the corresponding decrease in hysteresis width,  $\Delta F$  (from dark gray to light gray).

perennial or seasonal ice-cover at the pole disappears at  $F = F_w$ , and ice-cover reappears at the pole as  $F$  is ramped back down at  $F = F_c$ . The latter can be readily obtained analytically because it is the point of transition from an annually ice-free state, in which case the model equations are linear. The derivation is given in Appendix B. We find

$$F_c = A - \left[ F_b + (a_0 - a_2) \left( S_0 - S_1 \sqrt{1 + \tan^2 \phi + S_2} \right) \right], \quad (16)$$

where  $\phi = \tan^{-1}(\omega c_w/B) = 2.94$  months is the seasonal lag of the annually ice-free independent column at  $x = 1$ . The agreement between this exact solution and the numerical results is illustrated in Figure 6a.

Equation (16) indicates that  $F_c$  increases linearly with  $S_1$  (Figure 6a). This can be understood by considering that  $F = F_c$  is defined to be the point during a cooling scenario when ice first appears at the pole. This occurs when the winter minimum surface temperature crosses the freezing point, i.e., when ice appears on the coldest day of the year. Because the system is linear in the annually ice-free regime, the annual-mean value of  $E$  is linearly related to  $F$  whereas the seasonal amplitude of  $E$  is linearly related to  $S_1$ . The larger the seasonal amplitude of  $E$  is, the warmer the annual-mean value of  $E$  can be and still have the winter minimum satisfy  $E < 0$ . Hence, larger values of  $S_1$  are associated with larger values of  $F_c$ . This point is illustrated schematically in Figure 7 (blue shading).

An analogous argument applies to  $F_w$  (red shading in Figure 7), which indicates the transition point when an initially ice-covered pole is subjected to increasing  $F$ . When the seasonal amplitude ( $S_1$ ) increases, the warmest day of summer becomes ice-free at an earlier point, i.e., at a

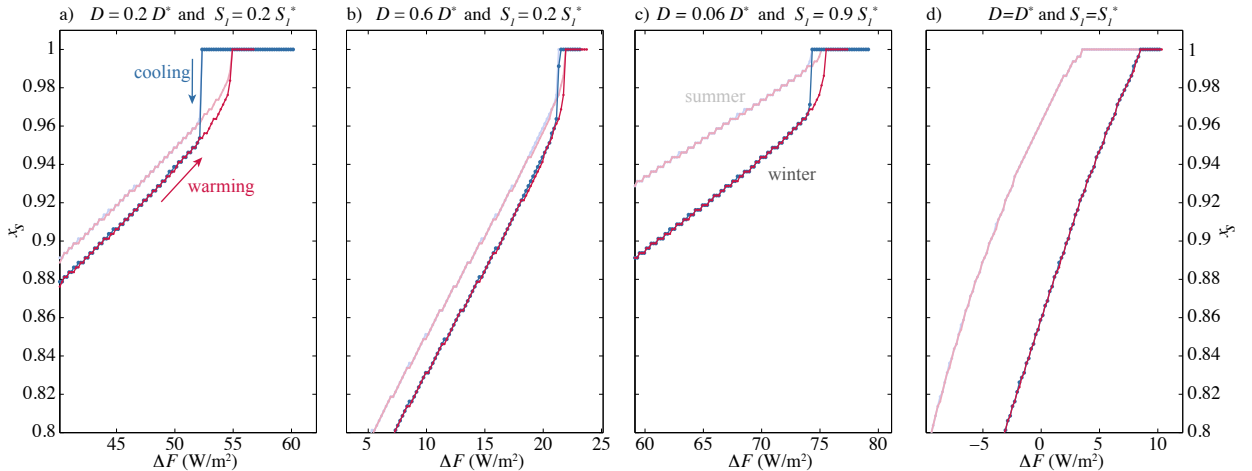


FIG. 8. Evolution of ice edge ( $x_i$ ) with forcing ( $F$ ) for warming (red) and cooling (blue) simulations. (a)–(d) Different values of the parameters ( $D$ ,  $S_1$ ). The winter ice edge is plotted in dark colors and the summer ice edge is plotted in faint colors. The vertical range includes only high latitudes. The slight jaggedness of the curves is related to the numerical horizontal resolution, with jumps occurring as the ice edge transitions from one model grid box to the next.

smaller value of  $F$ . At this point, the ice-albedo feedback causes an abrupt transition to an annually ice-free state. The relation between  $F_w$  and  $S_1$  is nonlinear due to the nonlinearity of the equations when ice is present.

The abrupt transition to an annually ice-free state occurs because the present model does not permit stable seasonally ice-free conditions at the pole with  $D = 0$  unless  $S_1$  is increased beyond the default value (not shown). This is consistent with the difficulties that SCMs have in obtaining stable seasonal ice (see Section 3), but it is in contrast with the results of some SCMs that do simulate stable seasonal ice in their default parameter regimes (e.g., Eisenman and Wettlaufer 2009; Moon and Wettlaufer 2012). The latter discrepancy is expected to arise because SCMs typically include a seasonal cycle in longwave forcing, analogous to the seasonally-varying diffusive term in the present model, which is necessary for some SCMs to simulate stable seasonally ice-free conditions (Eisenman 2012).

Since increasing  $S_1$  causes  $F_c$  to increase monotonically and  $F_w$  to decrease monotonically, we find that the hysteresis width ( $\Delta F$ ) decreases monotonically with increasing seasonal amplitude ( $S_1$ ). Figure 6b shows that this decrease is approximately linear, as expected from Figure 6a (cf. Figure 9D of Eisenman 2012).

## 5. Bistability with both seasonal cycle and diffusion

In Section 4, we found bistability in parameter regimes with either  $D = 0$  or  $S_1 = 0$ . However, the results in Section 3b imply that there is no bistability when  $D$  and  $S_1$  are both set to their default values. This raises the question how spatial and seasonal variations impact the stabil-

ity of the system when they both occur together. In this section we vary both  $D$  and  $S_1$  simultaneously, considering how the hysteresis width  $\Delta F$  varies in the full  $(D, S_1)$  parameter space.

We begin by considering four different  $(D, S_1)$  parameter sets (Figure 8). As shown in Figure 8d, a significant sea ice seasonal cycle without hysteresis is found for  $(D = D^*, S_1 = S_1^*)$ , in agreement with the discussion above. The ice edge curves in the warming scenario (red) are identical to those shown in Figure 3. Comparing Figures 8a and 8c illustrates the direct effect of how an increased seasonal amplitude in solar forcing reduces the bistable regime and forces an increased sea ice seasonal cycle. The analogous effect due to increased diffusivity ( $D$ ) becomes evident from comparing Figures 8a and 8b. Both have the same seasonal amplitude ( $S_1$ ), but the diffusivity ( $D$ ) is larger in Figure 8b. Consistent with the behavior discussed in Section 4b for  $S_1 = 0$ , the hysteresis width is smaller for the case with larger  $D$ . It is telling that the seasonal cycle of the ice edge is larger in Figure 8b despite  $S_1$  being unchanged. This illustrates that the presence of horizontal heat transport amplifies the seasonal variation in the ice edge. This can be understood from the effect that increased diffusivity has on the latitudinal temperature profile: turning up  $D$  reduces the annual-mean equator-to-pole temperature gradient. A lower temperature gradient in turn enables a larger seasonal cycle in  $T$ , and with it in  $x_s$ , for the same  $S_1$ .

Next, we performed 441 model runs to explore the model behavior in the full  $(D, S_1)$  space. We used 21 evenly spaced values for  $D$  in the range  $[0, 1.3D^*] = [0, 0.8] \text{ W/m}^2/\text{K}$  and 21 evenly spaced values for  $S_1$  in the

interval  $[0, S_1^*] = [0, 268] \text{ W/m}^2$ . In each simulation,  $F$  was ramped up and then down, and  $\Delta F$  was computed. The results are illustrated in Figure 9a.

Figure 9a indicates that the inclusion of both spatial and seasonal variations leads to a substantial reduction in bistability or equivalently an increase in overall stability. Starting at  $(S_1 = S_1^*, D = 0)$  and adding a diffusivity of just  $D = 0.1D^*$  suffices to eliminate any hysteresis in the model. Starting at  $(S_1 = 0, D = D^*)$  and adding a seasonality of just  $S_1 = 0.2S_1^*$  also eliminates any hysteresis. Lastly, if both parameters are reduced by equal factors starting at  $(S_1 = S_1^*, D = D^*)$ , bistability does not occur until  $(D, S_1) < 0.3(D^*, S_1^*)$ .

An approximate representation of the variations in  $\Delta F$  is shown in Figure 9b to assist a physical interpretation. The approximation is generated by simply adding the dependence on  $D$  shown in Figure 5b to the dependence on  $S_1$  shown in Figure 6b. In other words, using the functional notation  $\Delta F(D, S_1)$  as a shorthand,  $\Delta F(D, S_1)$  is approximated in Figure 9b as  $\Delta F(D, 0) + \Delta F(0, S_1) - \Delta F(0, 0)$ . The first term is given by the analytical solution from (13), the second term is the numerical result because no analytical solution of  $F_c$  with  $D = 0$  was obtained, and the third term is the analytical expression (15). Negative values of  $\Delta F(D, S_1)$  that arise from this computation are treated as zero. Although Figure 9b does not exactly match Figure 9a, the resemblance between the two suggests that a partial understanding of the dependence of  $\Delta F$  on  $D$  and  $S_1$  can be obtained by considering the EBM and SCM regimes in isolation.

## 6. Conclusion

Previous studies using seasonally-varying SCMs and spatially-varying EBMs have found instabilities in the sea ice cover associated with the ice-albedo feedback. Studies using comprehensive GCMs, however, have not found such instabilities. Here we developed a model of sea ice and climate that includes variations in both spatial and temporal dimensions with seasonally-varying forcing. The model accounts for seasonally-varying vertical heat fluxes through the sea ice and changes in ice thickness as well as the meridional heat transport in the atmosphere. The governing equation is a partial differential equation in time and latitude.

In one parameter regime ( $D = 0$ ), we showed that the spatial dimension was removed and the model reduced to a standard SCM, which is represented as an ordinary differential equation in time. In another parameter regime ( $S_1 = 0$ ), we showed that the temporal dimension was removed and the model reduced to a standard EBM, which is represented as an ordinary differential equation in latitude. When we varied the parameters, we found that including representations of both seasonal and spatial variations causes the stability of the system to substantially

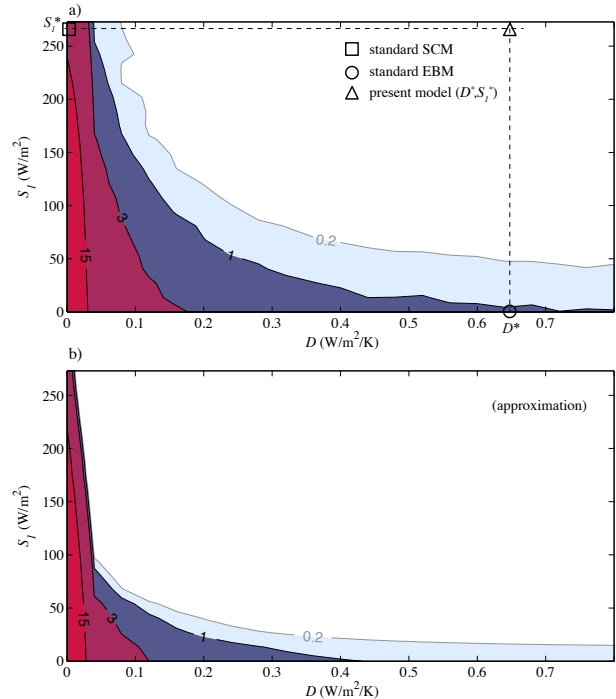


FIG. 9. Dependence of the stability of the ice cover ( $\Delta F$ ) on horizontal diffusivity ( $D$ ) and seasonal variations ( $S_1$ ), summarizing the main result of this study. (a) Result from 441 simulations of warming and then cooling. (b) Approximation generated by adding the results in Figures 5b and 6b, as discussed in the text.

increase (Figure 9a). This result may help to reconcile the discrepancy between low-order models and comprehensive GCMs in previous studies. Specifically, it suggests that the low-order models overestimate the likelihood of a sea ice “tipping point”.

It is worth emphasizing that this model contains substantial nonlinearity, including the ice-albedo effect and factors associated with sea ice thickness changes. Such nonlinearity has been shown in SCMs to lead to both accelerating sea ice loss and bifurcations. Nonetheless, the present model simulates a sea ice loss which not only involves no bifurcations but is also strikingly linear in the climate forcing (Figure 8d). This is in contrast with SCMs and EBMs and consistent with GCMs. The nonlinearities are essentially smoothed out when latitudinal and seasonal variations are included.

In addition to multiple sea ice states associated with the ice-albedo feedback, previous idealized modeling studies have demonstrated other processes in the climate system that are unstable in idealized low-order models but not in most comprehensive GCMs. Examples include the Atlantic Ocean meridional overturning circulation (Stommel 1961; Stouffer et al. 2006, e.g.,) and tropical monsoons (e.g. Zickfeld et al. 2005; Ma et al. 2014). Our results may

potentially have some bearing on these cases, although they do not indicate a general rule that allowing variations in more dimensions will necessarily stabilize a system.

*Acknowledgments.* The authors acknowledge ONR grant N00014-13-1-0469. I.E. further acknowledges NSF grant ARC-1107795.

## APPENDIX A

### Numerical integration of model

Here we discuss the numerical approach that we employ to solve the model (9)-(12). As mentioned above in Section 2e, in order to address the issue of diffusive heat transport between different surface temperature regimes, we create a system of equations representing two separate layers that are thermally coupled.

Diffusion takes place in a ‘‘ghost’’ layer with temperature  $T_g$  that evolves according to

$$c_g \frac{\partial T_g}{\partial t} = \frac{c_g}{\tau_g} (T - T_g) + D \nabla^2 T_g, \quad (\text{A1})$$

where  $c_g$  is the heat capacity of the ghost layer, and the first term on the right-hand side causes  $T_g$  to relax toward  $T$  with timescale  $\tau_g$ . All other processes occur in the main layer, whose surface enthalpy evolves as

$$\frac{\partial E}{\partial t} = C - B(T - T_m) - \frac{c_g}{\tau_g} (T - T_g), \quad (\text{A2})$$

which can be written as

$$\frac{\partial E}{\partial t} = C^* - M^* (T - T_m), \quad (\text{A3})$$

with

$$\begin{aligned} C^* &\equiv aS - A + F_b + F + \frac{c_g}{\tau_g} (T_g - T_m), \\ M^* &\equiv B + \frac{c_g}{\tau_g}. \end{aligned} \quad (\text{A4})$$

The temperature of the main layer,  $T$ , is as defined in (12) with

$$T_i = T_m + (C^* + F_b) \left( M^* + \frac{k}{h} \right)^{-1}. \quad (\text{A5})$$

To demonstrate the approximate equivalence between this two-layer system and the model described in Section 2a, we begin by defining a diffusive lengthscale associated with the diffusion operator in (A1),  $\delta x_D$  (cf. Lindzen and Farrell 1977; North 1984), and a timescale associated with changes in  $T$ ,  $\delta t_T$ . If  $\tau_g \ll c_g \delta x_D^2 / D$ , then the second term on the right-hand side of (A1) can be neglected, and if furthermore  $\tau_g \ll \delta t_T$ , then the relaxation timescale is sufficiently short that (A1) can be approximated by  $T_g = T$ .

Next, we add (A1) to (A2) to get

$$\frac{\partial E}{\partial t} + c_g \frac{\partial T_g}{\partial t} = C - B(T - T_m) + D \nabla^2 (T_g - T_m), \quad (\text{A6})$$

where we have used that  $\nabla^2 T_m = 0$ . Inserting  $T_g = T$  and the definition of  $E$  from equation (1), we see that the second term on the left-hand side of (A6) can be neglected as long as  $c_g \ll c_w$  in ice-free locations and  $c_g \ll L_f \delta h / \delta T_g$  in locations with ice, where  $\delta h$  and  $\delta T_g$  are scales of the variations of  $h$  and  $T_g$ . However, the first constraint on  $\tau_g$  imposes a lower limit on  $c_g$ , as becomes clear when rewriting the constraint as  $\tau_g / c_g \ll \delta x_D^2 / D$ . Hence in the limit of small  $c_g$ , small  $\tau_g$ , and small  $\tau_g / c_g$ , the two-layer system described in this section reduces to the model (9)-(12).

The two-layer system is considerably more amenable to numerical integration, so we use this for numerical solutions of the model after verifying that our values of  $\tau_g$  and  $c_g$  (see Table 1) are sufficiently small that reducing them does not substantially influence the solution.

We solve the two-layer system by integrating (A1) using the Implicit Euler method, since it is effective for solving the diffusion equation, and integrating (A2) using the Forward Euler method, since it is more straightforward for nonlinear systems. We use the same timestep,  $\Delta t$ , for both equations, which simplifies the coupling.

Numerically,  $T_g$  is given as a vector of length  $n$ , computed at each point in the domain  $x = [\Delta x / 2, 3\Delta x / 2, \dots, 1 - \Delta x / 2]$ , where  $\Delta x = 1/n$ . The diffusive term,  $D \nabla^2 T_g$ , is computed using the finite difference operator  $d_{j,k}$  for the Laplacian, where  $d_{j,k}$  is a matrix with elements

$$\begin{aligned} d_{j,j-1} &= \lambda_{j-1}, & j &= [2, n] & \text{(sub-diagonal)} \\ d_{j,j} &= -(\lambda_{j-1} + \lambda_j), & j &= [2, n-1] & \text{(diagonal)} \\ d_{j,j+1} &= \lambda_j, & j &= [1, n-1] & \text{(super-diagonal)} \end{aligned}$$

and diagonal end terms

$$d_{1,1} = -\lambda_1, \quad d_{n,n} = -\lambda_{n-1},$$

with  $\lambda_\alpha \equiv 1 / \Delta x^2 (1 - \tilde{x}_\alpha^2)$  and  $\tilde{x}_\alpha \equiv [0, \Delta x, \dots, 1 - \Delta x]$ . All other elements are zero, making  $d_{j,k}$  a tridiagonal matrix and hence rapidly invertible, which allows for efficient Implicit Euler time-stepping of (A1).

We further tested the numerical validity of this two-layer approach by removing the melting ice condition from (12), which creates an unphysical situation where the ice surface temperature is allowed to be greater than  $T_m$  but makes the system (9)-(12) more amenable to numerical integration. In this case, the one-layer system (9)-(12) can be directly solved by a single equation that represents an Implicit Euler time stepping of  $T$  where  $E > 0$  and a Forward Euler time stepping of  $h$  where  $E < 0$  (cf. Bitz and Roe accessed 2014). We verified the agreement between the one-layer and two-layer representations of the system, given this adjustment to (12).

APPENDIX B

Analytic expression for  $F_c$  when  $D = 0$

Here we derive the analytic expression (16), giving the critical forcing at which ice first appears at the pole in a cooling scenario in the limit of no heat transport ( $D = 0$ ). At the pole ( $x = 1$ ), the evolution of the system (9)–(12) under ice-free conditions is given by

$$c_w \frac{dT}{dt} = A_1 + A_2 \cos(\omega t) - B(T - T_m), \quad (\text{B1})$$

where

$$A_1 \equiv (a_o - a_2)(S_0 + S_2) - A + F_b + F,$$

$$A_2 \equiv (a_o - a_2)S_1.$$

Note that there is no spatial derivative in this case, since heat transport is set to zero. The solution to this linear system (B1) is

$$B(T - T_m) = A_1 + A_2 \frac{\cos(\omega t - \phi)}{\sqrt{1 + \tan^2 \phi}} \quad (\text{B2})$$

where  $\phi \equiv \tan^{-1}(\omega c_w / B)$  is the seasonal lag of the system as in Section 4. Solution (B2) ignores a transient term associated with the initial condition since we are considering a spun-up solution. Ice appears when the winter minimum value of  $T$  drops below  $T_m$ . This minimum occurs at  $t = \phi / \omega$ . Substituting this into (B2), setting  $T = T_m$ , and solving for the critical forcing  $F = F_c$ , leads to equation (16) in Section 4.

References

Abbot, D. S., and M. Silber, 2011: Bifurcations leading to summer Arctic sea ice loss. *J. Geophys. Res.*, **116**, D19 120.

Armour, K. C., I. Eisenman, E. Blanchard-Wrigglesworth, K. E. McCusker, and C. M. Bitz, 2011: The reversibility of sea ice loss in a state-of-the-art climate model. *Geophys. Res. Lett.*, **38**, L16 705.

Bitz, C. M., and G. H. Roe, 2004: A Mechanism for the High Rate of Sea Ice Thinning in the Arctic Ocean. *Journal of Climate*, **17** (18), 3623–3632.

Bitz, C. M., and G. H. Roe, accessed 2014: *Ice and Climate Modeling, Course Notes (2001)*. <http://www.atmos.washington.edu/bitz/seasonal.tar>.

Björk, G., 2002: Dependence of the Arctic Ocean ice thickness distribution on the poleward energy flux in the atmosphere. *J. Geophys. Res.*, **107** (C10), 3173.

Björk, G., C. Stranne, and K. Borenäs, 2013: The Sensitivity of the Arctic Ocean Sea Ice Thickness and Its Dependence on the Surface Albedo Parameterization. *Journal of Climate*, **26** (4), 1355–1370.

Budyko, M. I., 1969: The effect of solar radiation variations on the climate of the Earth. *Tellus*, **21** (5), 611–619.

Budyko, M. I., 1972: The future climate. *Eos, Trans. AGU*, **53** (10), 868.

Cahan, R. F., and G. R. North, 1979: A Stability Theorem for Energy-Balance Climate Models. *J Atmos Sci*, **36**, 1178–1188.

Croll, J., 1875: *Climate and Time in their Geological Relations*. Cambridge University Press, Cambridge.

Eisenman, I., 2007: Arctic catastrophes in an idealized sea ice model. *2006 Program of Studies: Ice (Geophysical Fluid Dynamics Program)*, Woods Hole, Mass., Woods Hole Oceanogr. Inst., 133–161.

Eisenman, I., 2010: Geographic muting of changes in the Arctic sea ice cover. *Geophys. Res. Lett.*, **37** (16), L16 501.

Eisenman, I., 2012: Factors controlling the bifurcation structure of sea ice retreat. *J. Geophys. Res.*, **117** (D1), D01 111.

Eisenman, I., and J. S. Wettlaufer, 2009: Nonlinear threshold behavior during the loss of Arctic sea ice. *Proceedings of the National Academy of Sciences*, **106** (1), 28–32.

Flato, G. M., and R. D. Brown, 1996: Variability and climate sensitivity of landfast Arctic sea ice. *J. Geophys. Res.*, **101** (C11), 25 767.

Gregory, J. M., 2002: Recent and future changes in Arctic sea ice simulated by the HadCM3 AOGCM. *Geophys. Res. Lett.*, **29** (24), 2175.

Held, I. M., and M. J. Suarez, 1974: Simple albedo feedback models of the icecaps. *Tellus*, **26** (6), 613–629.

Hunt, B., 1984: Polar glaciation and the genesis of ice ages. *Nature*, **308**, 48–51.

Langen, P. L., and V. A. Alexeev, 2004: Multiple equilibria and asymmetric climates in the CCM3 coupled to an oceanic mixed layer with thermodynamic sea ice. *Geophys. Res. Lett.*, **31**, L04 201.

Li, C., D. Notz, S. Tietsche, and J. Marotzke, 2013: The Transient versus the Equilibrium Response of Sea Ice to Global Warming. *Journal of Climate*, **26** (15), 5624–5636.

Lian, M. S., and R. D. Cess, 1977: Energy Balance Climate Models: A Reappraisal of Ice-Albedo Feedback. *J Atmos Sci*, **34** (7), 1058–1062.

Lindzen, R. S., and B. Farrell, 1977: Some Realistic Modifications of Simple Climate Models. *J Atmos Sci*, **34** (10), 1487–1501.

Ma, D., W. Boos, and Z. Kuang, 2014: Effects of Orography and Surface Heat Fluxes on the South Asian Summer Monsoon. *Journal of Climate*, **27** (17), 6647–6659.

Maykut, G. A., and M. G. McPhee, 1995: Solar heating of the Arctic mixed layer. *J. Geophys. Res.*, **100** (C12), 24 691.

Maykut, G. A., and N. Untersteiner, 1971: Some results from a time-dependent thermodynamic model of sea ice. *J. Geophys. Res.*, **76** (6), 1550–1575.

Mengel, J. G., D. A. Short, and G. R. North, 1988: Seasonal snow-line instability in an energy balance model. *Climate Dynamics*, **2** (3), 127–131.

Moon, W., and J. S. Wettlaufer, 2011: A low-order theory of Arctic sea ice stability. *EPL*, **96** (3), 39 001.

Moon, W., and J. S. Wettlaufer, 2012: On the existence of stable seasonally varying Arctic sea ice in simple models. *J. Geophys. Res.*, **117**, C07 007.

- Müller-Stoffels, M., and R. Wackerbauer, 2011: Regular network model for the sea ice-albedo feedback in the Arctic. *Chaos*, **21** (1), 013–111.
- Müller-Stoffels, M., and R. Wackerbauer, 2012: Albedo parametrization and reversibility of sea ice decay. *Nonlinear Proc. Geophys.*, **19** (1), 81–94.
- North, G. R., 1975a: Analytical Solution to a Simple Climate Model with Diffusive Heat Transport. *J Atmos Sci*, **32** (7), 1301–1307.
- North, G. R., 1975b: Theory of energy-balance climate models. *J Atmos Sci*, **32** (11), 2033–2043.
- North, G. R., 1984: The Small Ice Cap Instability in Diffusive Climate Models. *J Atmos Sci*, **41** (23), 3390–3395.
- North, G. R., R. F. Cahalan, and J. A. Coakley, Jr., 1981: Energy balance climate models. *Reviews of Geophysics*, **19** (1), 91.
- North, G. R., and J. A. Coakley, Jr., 1979: Differences between Seasonal and Mean Annual Energy Balance Model Calculations of Climate and Climate Sensitivity. *J Atmos Sci*, **36**, 1189–1204.
- Ridley, J., J. Lowe, and D. Simonin, 2007: The demise of Arctic sea ice during stabilisation at high greenhouse gas concentrations. *Climate Dynamics*, **30** (4), 333–341.
- Ridley, J. K., J. A. Lowe, and H. T. Hewitt, 2012: How reversible is sea ice loss? *The Cryosphere*, **6**, 193–198.
- Sellers, W. D., 1969: A Global Climatic Model Based on the Energy Balance of the Earth-Atmosphere System. *Journal of Applied Meteorology*, **8** (3), 392–400.
- Stommel, H., 1961: Thermohaline Convection with Two Stable Regimes of Flow. *Tellus*, **13** (2), 224–230.
- Stouffer, R. J., and Coauthors, 2006: Investigating the causes of the response of the thermohaline circulation to past and future climate changes. *Journal of Climate*, **19** (8), 1365–1387.
- Thorndike, A. S., 1992: A toy model linking atmospheric thermal radiation and sea ice growth. *J. Geophys. Res.*, **97** (C6), 9401.
- Tietsche, S., D. Notz, J. Jungclaus, and J. Marotzke, 2011: Recovery mechanisms of arctic summer sea ice. *Geophysical Research Letters*, **38** (2).
- Winton, M., 2006: Does the Arctic sea ice have a tipping point? *Geophys. Res. Lett.*, **33**, L23 504.
- Winton, M., 2008: Sea Ice-Albedo Feedback and Nonlinear Arctic Climate Change. *Arctic sea ice decline: Observations, projections, mechanisms, and implications*, AGU, Washington, D.C., 111–131.
- Winton, M., 2011: Do Climate Models Underestimate the Sensitivity of Northern Hemisphere Sea Ice Cover? *Journal of Climate*, **24**, 3924–3934.
- Zickfeld, K., B. Knopf, and V. Petoukhov, 2005: Is the Indian summer monsoon stable against global change? *Geophys. Res. Lett.*, **32**, L15 707.